≋AGU PUBLICATIONS

Geophysical Research Letters

RESEARCH LETTER

Key Points:
- Proximity of 2013 and 2015 events enabled spectral deconvolution of tsunami waveforms to estimate 2013 source periods of 10 and 22 min
- High rupture velocity of 3.6 km/s on north dipping normal-fault plane for the 2015 Solomon Islands earthquake
- Positive stress transfer by the 2013 Santa Cruz earthquake to the 2015 Solomon Islands earthquake

Supporting Information:
- Supporting Information S1

Correspondence to:
M. Heidarzadeh,
heidarzadeh@pari.go.jp

Citation:
Heidarzadeh, M., T. Harada, K. Satake, T. Ishibe, and A. R. Gusman (2016), Comparative study of two tsunamigenic earthquakes in the Solomon Islands: 2015 M_w 7.0 normal-fault and 2013 Santa Cruz M_w 8.0 megathrust earthquakes, *Geophys. Res. Lett.*, 43, doi:10.1002/2016GL068601.

Comparative study of two tsunamigenic earthquakes in the Solomon Islands: 2015 M_w 7.0 normal-fault and 2013 Santa Cruz M_w 8.0 megathrust earthquakes

Mohammad Heidarzadeh[1,2], **Tomoya Harada**[2], **Kenji Satake**[2], **Takeo Ishibe**[3], and **Aditya Riadi Gusman**[2]

[1]Port and Airport Research Institute, Yokosuka, Japan, [2]Earthquake Research Institute, University of Tokyo, Tokyo, Japan, [3]Association for the Development of Earthquake Prediction, Tokyo, Japan

Abstract The July 2015 M_w 7.0 Solomon Islands tsunamigenic earthquake occurred ~40 km north of the February 2013 M_w 8.0 Santa Cruz earthquake. The proximity of the two epicenters provided unique opportunities for a comparative study of their source mechanisms and tsunami generation. The 2013 earthquake was an interplate event having a thrust focal mechanism at a depth of 30 km while the 2015 event was a normal-fault earthquake occurring at a shallow depth of 10 km in the overriding Pacific Plate. A combined use of tsunami and teleseismic data from the 2015 event revealed the north dipping fault plane and a rupture velocity of 3.6 km/s. Stress transfer analysis revealed that the 2015 earthquake occurred in a region with increased Coulomb stress following the 2013 earthquake. Spectral deconvolution, assuming the 2015 tsunami as empirical Green's function, indicated the source periods of the 2013 Santa Cruz tsunami as 10 and 22 min.

1. Introduction

A tsunamigenic earthquake occurred on 18 July 2015 in the Solomon Islands, southwestern Pacific Ocean (Figure 1). The epicenter was at 165.172°E and 10.444°S with a depth of 10.0 km and a moment magnitude, M_w, of 7.0 according to the United States Geological Survey (USGS). A normal-fault mechanism was reported by USGS. The Pacific Tsunami Warning Center issued a tsunami alert, but it was lifted shortly afterward because coastal observations showed small sea level fluctuations with amplitudes up to ~10 cm.

The southwestern Pacific Ocean accommodates a complex tectonic setting including several tectonic plates forming a number of convergent and divergent plate boundaries. The Solomon Islands earthquake of July 2015 occurred near the easternmost of the Solomon Islands trench and the northern end of the Vanuatu trench (also known as New Hebrides trench) which form the convergent boundaries between the Pacific and Australian Plates (Figure 1). The epicentral area is an active subduction zone having produced several tens of $M > 7$ earthquakes since around 100 years ago. The region experienced a large thrust earthquake (M_w 8.0) on 6 February 2013 (known as the Santa Cruz earthquake) generating a tsunami that caused 10 deaths [*Fritz et al.*, 2014; *Lay et al.*, 2013; *Romano et al.*, 2015]. Another large M_w 8.1 thrust earthquake on 1 April 2007 also produced a regional tsunami with 52 deaths (Figure 1) [*Fritz and Kalligeris*, 2008; *Chen et al.*, 2009; *Taylor et al.*, 2008; *Wei et al.*, 2015]. This region also has the potential to produce tsunami earthquakes; a moderate M_w 7.1 tsunami earthquake on 3 January 2010 produced large runup heights of up to 7 m [*Newman et al.*, 2011] (Figure 1). The hypocenter of the July 2015 earthquake indicates that this normal-fault earthquake occurred within the overriding Pacific Plate at a shallow depth of 10 km (inset in Figure 1).

Although the July 2015 tsunamigenic earthquake had a moderate size (i.e., M_w 7.0), it is an important and unique event both regionally and globally in various ways:

1. It is an example of normal-fault earthquakes in the overriding plate which are very rare. Another example is the 11 April 2011 Fukushima M_w 6.6 earthquake which occurred far inland without generating a tsunami [*Tanaka et al.*, 2014; *Ishibe et al.*, 2015]. Tsunamis from normal-fault earthquakes have been reported offshore Kuril in 2007 (M_w 8.1) [*Rabinovich et al.*, 2008; *Fujii and Satake*, 2008], offshore Indonesia in August 1977 (M_w 8.3) [*Gusman et al.*, 2009], offshore Samoa Islands in September 2009 [*Okal et al.*, 2010; *Fritz et al.*, 2011; *Beavan et al.*, 2010], and offshore Japan in March 1933 (M_w 8.6) [*Tanioka et al.*, 1997], but all these events occurred within the subducting oceanic plate.
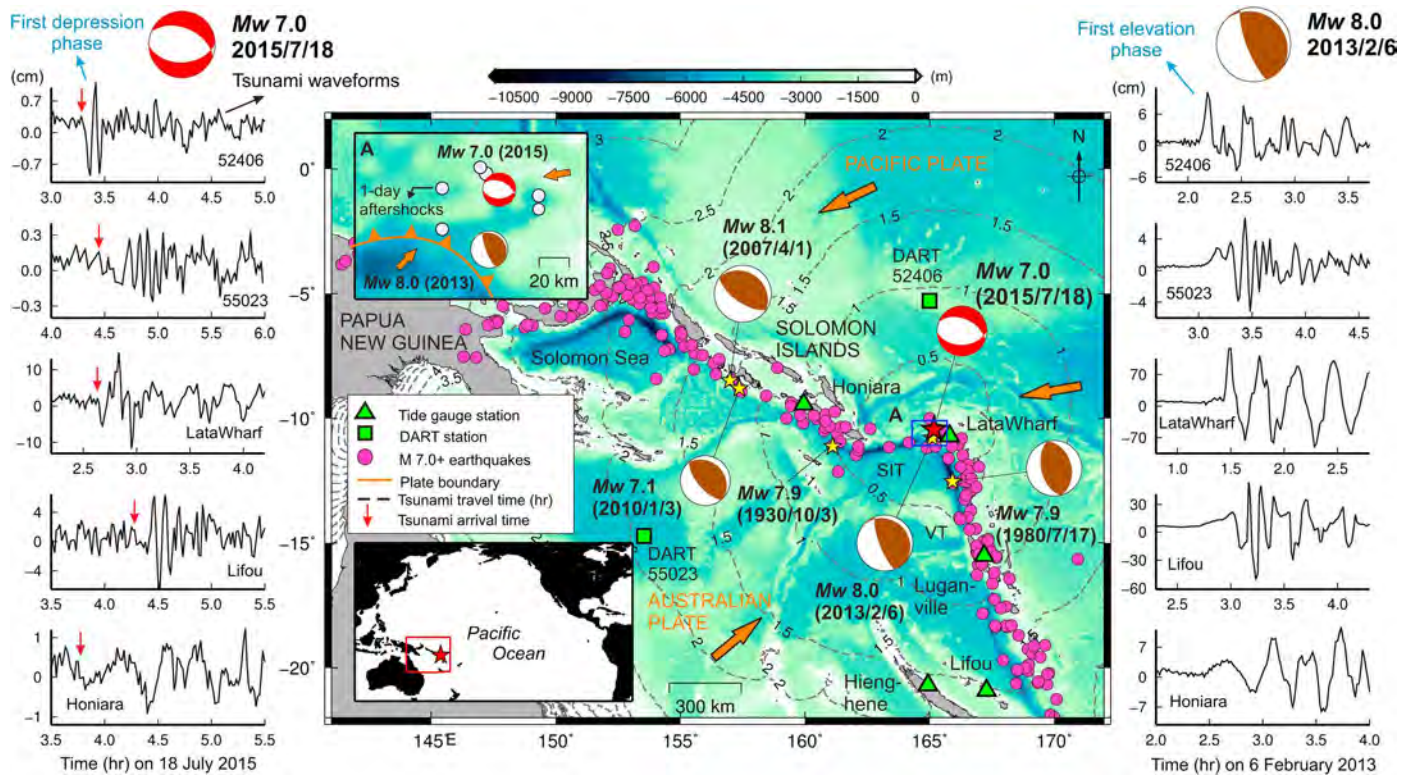
Figure 1. Epicentral area, tectonic setting, and sea level stations. The USGS earthquake catalog is utilized for the epicenters of $M > 7.0$ earthquakes since A.D. 1900. *Nakanishi and Kanamori* [1984] provided the focal mechanism for the 1980 earthquake. For focal mechanisms of other earthquakes, we used USGS catalog. Dashed lines are tsunami travel times for the 2015 earthquake. The waveforms shown on left and right sides are for the 2015 and 2013 tsunamis, respectively. The red arrows indicate expected tsunami arrival time at each station. Abbreviations: SIT, Solomon Islands Trench; VT, Vanuatu Trench.

2. The occurrence of this moderate tsunamigenic earthquake was possibly facilitated by stress transfer from the 2013 Santa Cruz earthquake. We explore this possibility through Coulomb stress transfer and seismicity rate analyses. This event provides another example for the concept of Coulomb stress transfer [e.g., *Stein*, 1999]. Stressing of overriding plates during earthquake cycles is discussed by *Taylor et al.* [1996] and *Zheng et al.* [1996].

3. As the sources of the 2015 Solomon Islands and 2013 Santa Cruz tsunamis are very close to each other (~40 km, Figure 1), the former smaller tsunami may serve as empirical Green's function for the latter larger one. Hence, spectral deconvolution results in the source spectrum of the 2013 Santa Cruz tsunami. Empirical Green's functions have been applied to seismic waveform data [e.g., *Hartzell*, 1978] but have never been applied for tsunamis.

The overall objective of this work was to compare the 2013 and 2015 Solomon Islands earthquakes and tsunamis. The proximity of the 2013 and 2015 epicenters (~40 km) provided unique opportunities to investigate the relationship between them using tsunami and seismic data. We obtained both tsunami and teleseismic records of the 18 July 2015 tsunami and earthquake and conducted numerical tsunami simulations, teleseismic body wave inversion, tsunami spectral deconvolution, Coulomb stress transfer analysis, and seismicity analysis. Our aims were the following: (1) to obtain a rupture model for the 2015 earthquake, (2) to study seismicity and Coulomb stress transfer from the 2013 Santa Cruz earthquake, and (3) to explore the source spectrum of the 2013 tsunami by applying spectral deconvolution.

2. Data and Methods

Source models of earthquakes have been estimated using various data including teleseismic, near-field strong motion, tsunami, and geodetic records [e.g., *Koketsu et al.*, 2011]. Among various data, the nature of tsunami data is different from that of seismic data because seismic waves propagate ~ 20–100 times faster

than those of tsunami. Due to such a large difference in travel speeds, seismic data give high temporal resolution of the source process whereas tsunami waveforms allow a reliable spatial distribution for the tsunami source, as first reported by *Satake* [1987]. A more accurate slip distribution for tsunamigenic earthquakes can be achieved by a combined use of both tsunami and seismic data in order to maintain high-resolution solutions both in time and space domains [e.g., *Gusman et al.*, 2015; *Lay et al.*, 2014; *Heidarzadeh et al.*, 2015, 2016].

The data consist of 71 teleseismic records and 7 tsunami records. The teleseismic records were collected from the Incorporated Research Institutions for Seismology; all located in the far-field (distance range of 30°–100° from the epicenter) with full azimuthal coverage (Figure S1 in the supporting information). We band-pass filtered the vertical component records for the band 0.004–1.0 Hz. Out of seven tsunami records, two were Deep-ocean Assessment and Reporting of Tsunamis (DART) records coming from the U.S. National Oceanic and Atmospheric Administration and five were tide gauge records from the Intergovernmental Oceanographic Commission. All tsunami stations were located outside the area of seafloor deformation. Tsunami records were sampled at 1 min intervals. We estimated the tidal signals using polynomial fitting and removed them from tsunami records. For spectral analysis, we exploited the Welch's averaged modified-periodogram method [*Welch*, 1967].

We performed teleseismic body wave inversions by employing the method by *Kikuchi and Kanamori* [1991] using P wave records to obtain slip distribution. We utilized the velocity structures of CRUST 2.0 and ak135 [*Bassin et al.*, 2000; *Kennett et al.*, 1995]. The focal mechanism solution reported by Global Centroid Moment Tensor (GCMT) solution as strike: 88.0°, dip: 44.0°, and rake: −108.0° (NP-1), and strike: 291.0°, dip: 49.0°, and rake: −74.0° (NP-2) were used. For each subfault, with size of 5 km × 5 km, we allowed maximum rupture duration of 4.0 s forming from three rise-time triangles with duration of 2 s overlapped by 1.0 s. We changed rupture velocity (V_r) in the range of 1.6–4.0 km/s with 0.2 km/s intervals, yielding 13 different solutions for each nodal plane. Due to the variable V_r, the number of subfaults was ranged from 11 (along strike) × 5 (along dip) to 19 × 6. The teleseismic body wave inversion applied here is not the same as typical teleseismic inversion which is based on a single V_r. Our method, which was previously applied by *Lay et al.* [2014] and *Gusman et al.* [2015], uses a variable maximum V_r in order to examine which source model gives better agreement with tsunami data.

Tsunami simulations were conducted using the nonlinear shallow water model of *Satake* [1995]. The 30 arc sec GEBCO digital bathymetry data were used [*Intergovernmental Oceanographic Commission et al.*, 2003]. We utilized a time step of 1.0 s. Analytical formulas of *Okada* [1985] were employed for calculations of coseismic seafloor deformation. While various slip distributions obtained by teleseismic inversion with different rupture velocities were used as initial condition, rupture velocity was not considered in tsunami simulation. Tsunami travel time calculation was performed by the TTT software [*Geoware*, 2011]. Quality of fit between simulations and observations was measured using normalized root-mean-square (NRMS) misfit [*Heidarzadeh et al.*, 2016]. We used the first wave cycle of tsunami at each station for NRMS calculations. The NRMS misfits from tsunami and teleseismic simulations can be compared to each other because they are normalized with the amplitudes of the observations.

Stress transfer analysis was performed by calculating static changes of the Coulomb failure stress, known as ΔCFF, which is defined as $\Delta CFF = \Delta\tau - \mu'\Delta\sigma$, where $\Delta\tau$ and $\Delta\sigma$ are the shear and normal stress changes, respectively, and μ' is the apparent friction coefficient [*Stein et al.*, 1992; *Ishibe et al.*, 2015]. Regions with positive and negative ΔCFF values indicate regions with increased and decreased Coulomb stress following the earthquake, respectively. In order to consider spatial heterogeneity of stress fields, ΔCFF calculations were conducted by using the focal mechanism of each earthquake as the receiver fault [*Ishibe et al.*, 2011]. We used the heterogeneous fault slip model of the 2013 Santa Cruz earthquake by *Lay et al.* [2013] and focal mechanism solutions of earthquakes between 1 January 2010 and the 18 July 2015 Solomon Islands earthquake among the GCMT catalog in order to evaluate ΔCFF transferred from the 2013 Santa Cruz earthquake. The total number of GCMT solutions was 241. We assumed an elastic half-space model and used an apparent friction coefficient of 0.4, a Poisson ratio of 0.25, and a rigidity of 40 GPa for the earth.

3. Source Model of the July 2015 Earthquake

Finite-fault inversions for 13 rupture velocities and 2 nodal planes showed that they are similar to each other concerning the match between the observed and synthetic seismic waveforms. Examples of the results are
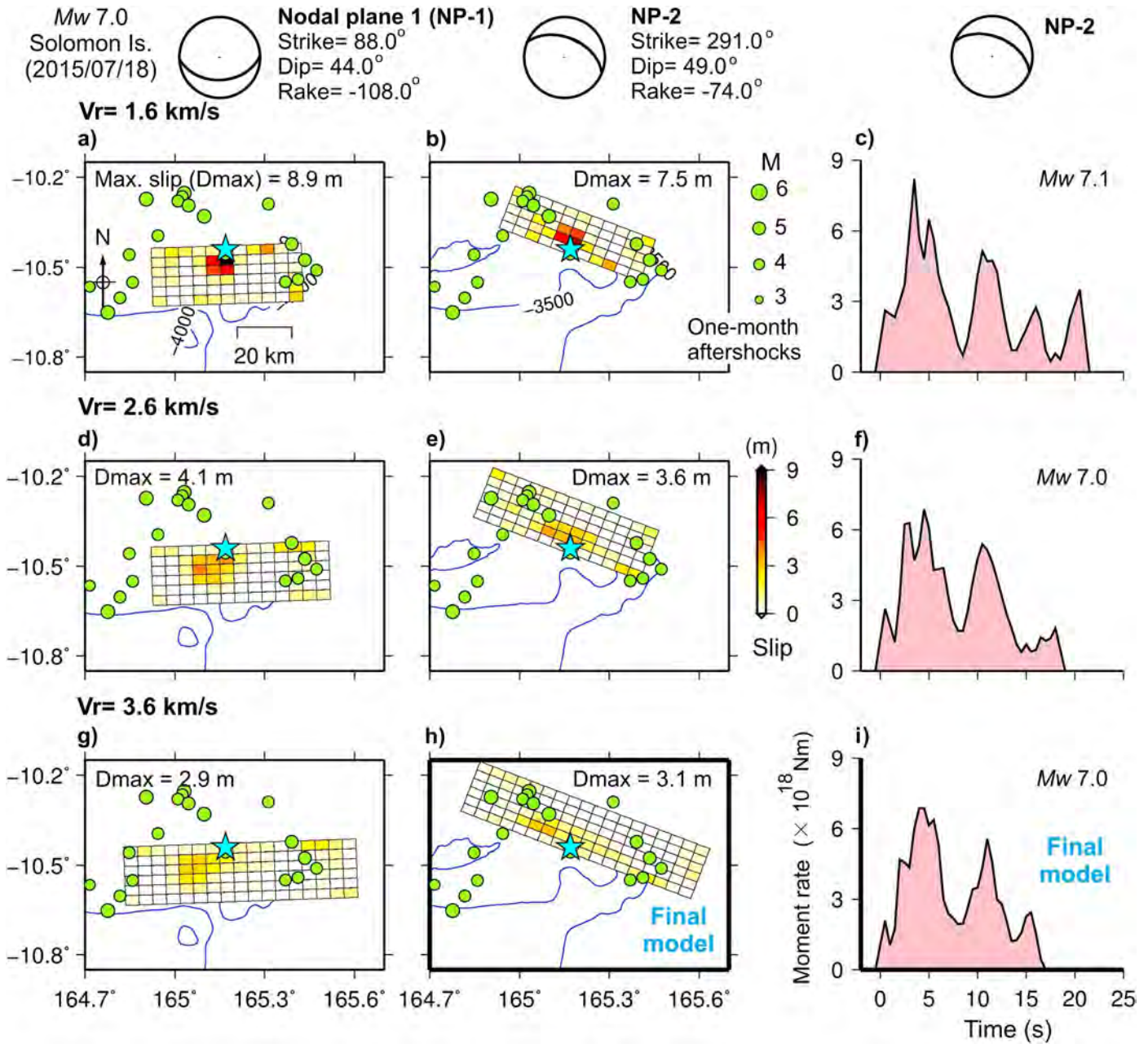
Figure 2. Results of teleseismic body wave inversions. (a–i) Slip distributions on both nodal planes (NP-1 and NP-2) and source time functions (moment-rate functions) on NP-2 for three different rupture velocities. Aftershocks, occurred within 1 month after the 2015 Solomon Islands earthquake, are also plotted. Blue contours show water depth.

shown for V_r = 1.6 and 3.6 km/s for the NP-2 (Figures S2 and S3). Although the rupture velocities are very different for these two cases, the resulting synthetic waveforms are similar. The NRMS misfits for teleseismic results were very close to each other for both nodal planes and were in the small ranges of 0.636–0.656 and 0.654–0.671 for NP-1 and NP-2, respectively (Figure 3e). In addition, the curves of the NRMS misfits were flat without distinct trough. Therefore, it was challenging to choose the best model out of the 26 models from teleseismic results. Nonetheless, the spatial slip distributions and the maximum slip amounts are different for various models and nodal planes (Figures 2 and S4). When rupture velocity increases, the ruptured areas expand but the maximum slip decreases (Figures 2 and S4). We thus simulate tsunamis from these different slip models and compare the synthetic tsunami waveforms.

F2
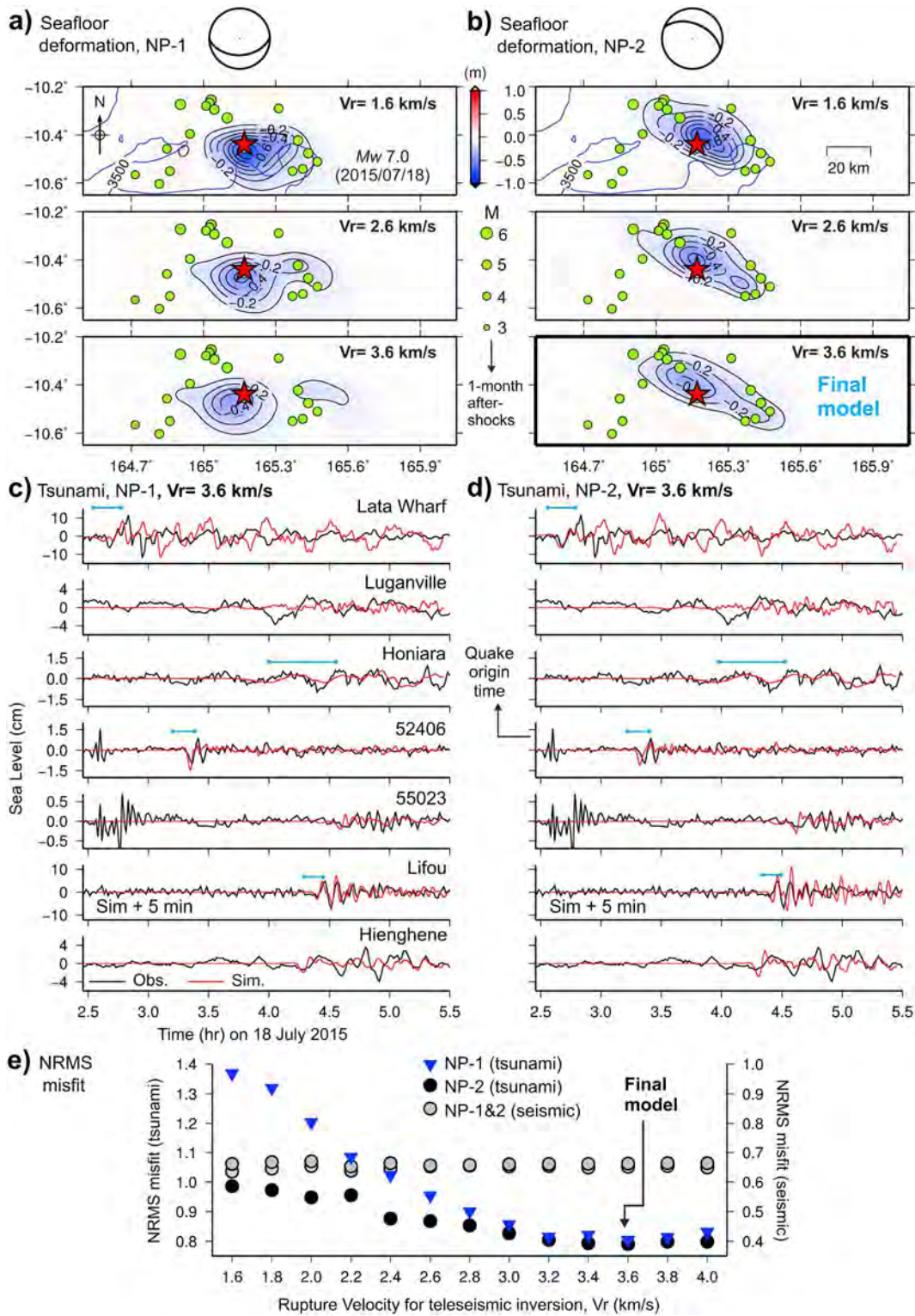
Figure 3. (a, b) Seafloor deformation for various models and nodal planes. The black contours show seafloor deformation and start from 0.1 m with 0.1 m intervals. Blue contours show water depth. (c) Comparison of the observations (black) and simulations (red) for the slip distribution model with $V_r = 3.6$ km/s on NP-1. The simulated waveforms for Lifou were shifted 5 min to match with the observations. Horizontal blue lines show part of the tsunami records considered for NRMS misfit computations. (d) Same as Figure 3c but for the model with $V_r = 3.6$ km/s on NP-2 which is our final model. (e) NRMS misfits for various slip models. Rupture velocity was varied in teleseismic inversion to estimate the slip distribution, which was then used for tsunami simulations.

Tsunami simulations revealed that the synthetic tsunami waveforms were significantly different for 26 models (Figure S6 shows tsunami simulations for 13 models of NP-2). We note that we did not change the rupture velocity for tsunami simulations; instead, we employed various slip distribution models obtained from teleseismic inversions using different V_r. The simulated tsunami amplitudes from the slip distribution of seismic model of $V_r = 1.6$ km/s (Figure S6a) are around twice larger than those of model $V_r = 4.0$ km/s at some locations (Figure S6m). This implies that tsunami simulation is capable of differentiating between available models although the fit between the observed and simulated tsunami waveforms is not as good as that of seismic waveforms. The NRMS misfits for tsunami indicate that NP-2 gives smaller misfits compared to NP-1 (Figure 3e). The slip distribution for $V_r = 3.6$ km/s is the best one as it gives the minimum value of the NRMS misfit for both nodal planes (Figure 3e). The NRMS misfit curve becomes flat beyond the slip distribution with V_r of 3.2 km/s indicating that tsunami simulations favor fault models of $V_r > 3.2$ km/s. The NP-2 appears to be the fault plane because, first, it results in smaller NRMS misfits than NP-1(Figure 3e) and, second, it is more consistent with spatial distribution of aftershocks (Figures 2 and 3). Our final slip model, based on the seismic and tsunami waveform analyses, is on the north dipping nodal plane (NP-2) having a rupture velocity of 3.6 km/s (Figure 2h). The total duration of rupture is ~17 s having the peak at ~5 s (Figure 2i). The average slip is 0.6 m, and the large-slip area (areas having slips >1.5 times of the average slip, *Murotani et al.* [2013]) was 35 km (along strike) × 10 km (along dip). The maximum seafloor uplift and subsidence are ~4 and ~42 cm, respectively. The seismic moment is 4.21×10^{19} Nm giving M_w 7.0.

4. Stress Transfer From the 2013 Santa Cruz Earthquake

Great interplate earthquakes sometimes induce shallow normal-fault earthquakes in the surrounding areas [e.g., *Ammon et al.*, 2008; *Kato et al.*, 2011; *Ishibe et al.*, 2015]. For the Solomon Islands region, seismicity analysis revealed that regional seismicity significantly increased following the 6 February 2013 Santa Cruz earthquake, and temporal distribution of the seismicity showed that level of the seismicity is still high after more than two years relative to that before the 2013 event (Figures S8c and S8d). Coulomb stress transfer analysis showed that ΔCFF from the 2013 Santa Cruz earthquake is positive around the hypocenter of the 2015 Solomon Islands earthquake when the NP-2 of the 2015 event is assumed as the receiver fault (Figures 4b and 4c). We also calculated ΔCFF for GCMT solutions of 241 earthquakes before and after the 2013 event using their own focal mechanisms as the receiver faults (Figures 4d and 4e). Normal-fault earthquakes, according to *Frohlich* [1992] classifications, occurred with a rate of 7.1 event/yr before the 2013 earthquake and 22.9 event/yr after that, indicating a significant increase. Among 56 normal-fault earthquakes which occurred after the 2013 Santa Cruz event, 50 of them (~90%) received positive ΔCFF from the Santa Cruz event for at least one of their nodal planes (Figures 4d and 4e). These results suggest that the Coulomb stress changes imparted by the 2013 Santa Cruz earthquake possibly facilitated the generation of the 2015 Solomon Islands earthquake with normal-fault mechanism, although the two events were more than two years apart. The analyses were repeated for different values of apparent friction coefficient (μ') and for both nodal planes (Figure S7) revealing that the results were robust.

5. Source Spectrum of the 2013 Santa Cruz Earthquake

Following the occurrence of tsunamigenic earthquakes, the resulting tsunami waves propagate through various submarine bathymetric features and are refracted and reflected from coastlines until they are recorded at sea level stations [e.g., *Satake*, 1988]. Therefore, the tsunami records on DART or tide gauge stations contain a history of tsunami propagation effects in addition to tsunami source features. Here we call such features as tsunami propagation-path effects. For example, the tsunami spectra at the Lata Wharf station showed similar peak at ~20 min for both the 2013 and 2015 tsunamis although the latter tsunami was much smaller than the former one (point A in Figures 5c and 5d). This is possibly a propagation-path effect. If two tsunamis, with different powers, occur close to each other at different times, the smaller event may serve as empirical Green's function for the larger one. Therefore, for the larger event, spectral deconvolution separates the propagation-path effects from the tsunami records and gives the source spectrum of the tsunami [e.g., *Rabinovich*, 1997; *Heidarzadeh and Satake*, 2014]. In other words, the smaller tsunami helps to remove the propagation-path effects from the tsunami records of the larger event as long as the source periods of the smaller event are shorter than those of the larger one.
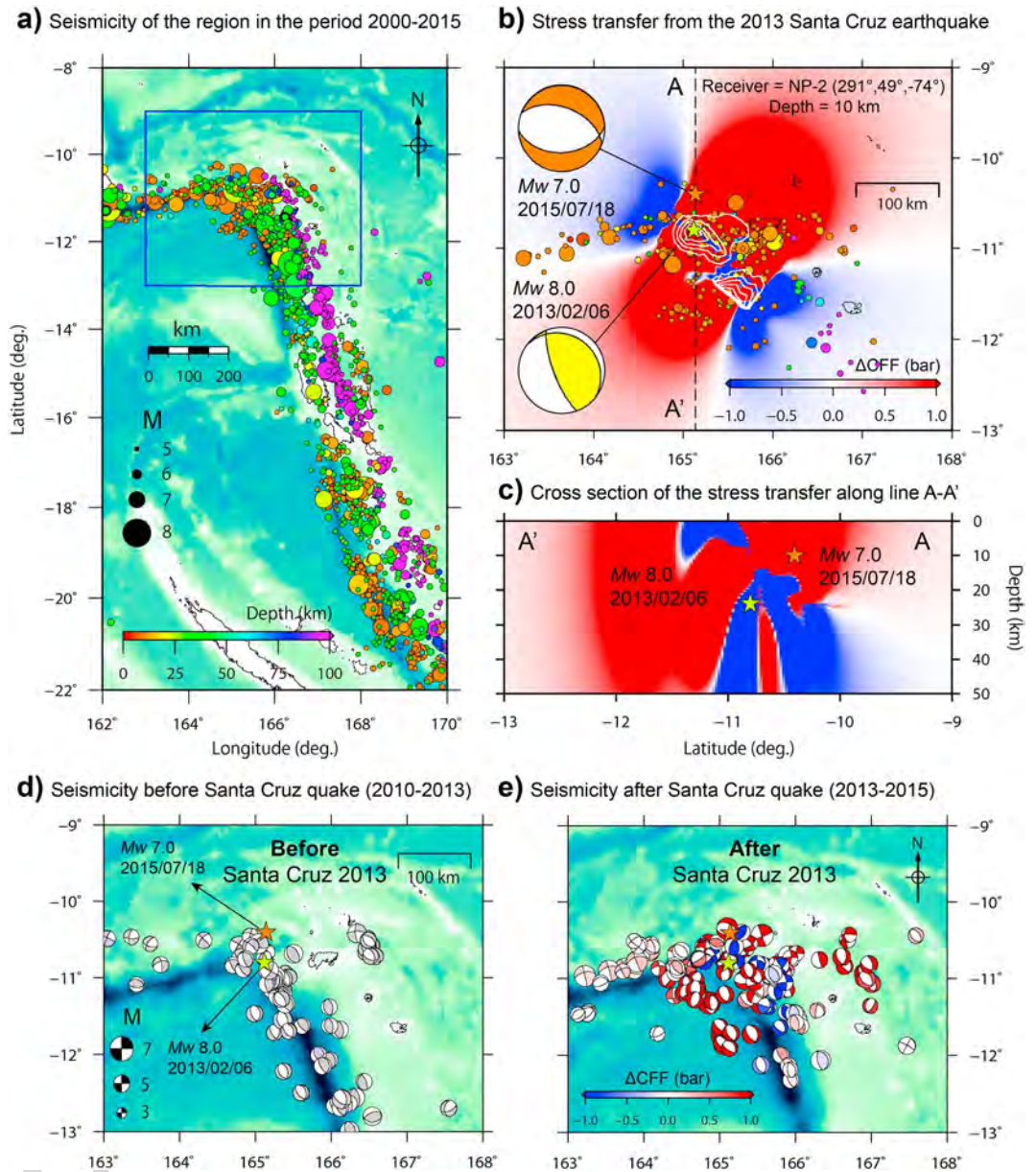
Figure 4. (a) Seismicity of the Solomon Islands region in past 15 years (period 2000–2015). Data are from USGS. (b) ΔCFF from the 2013 earthquake for the receiver fault of the 2015 earthquake (NP-2). Slip distribution of the 2013 earthquake (white contours) is from *Lay et al.* [2013]. Contours of slip distribution begin from 2 m with 2 m intervals. The seismicity shown in this panel is for the period from 6 February 2013 to 18 July 2015. (c) Vertical distribution of ΔCFF along the line A-A'. (d and e) Seismicity and focal mechanism solutions (from GCMT catalog) for time periods of before and after the 2013 earthquake. The color in focal mechanism solutions indicate computed ΔCFF assuming each focal mechanism as the receiver fault for NP-2.

Here as the sources of the two tsunamis of 2015 and 2013 are very close to each other (~40 km apart, Figure 1) and the latter is much larger than the former one (Figures 5a and 5b), the 2015 tsunami serves as empirical Green's function for the 2013 one. Because it is the first time that empirical Green's function method is adopted for tsunamis, it is useful to compare the results from this method with previous results. Figures 5a and 5b show that the propagation paths of the two tsunamis are similar. Spectral deconvolution is usually conducted using spectral division. The peaks of the spectral-ratio plot give the tsunami source spectrum of the larger event. Figure 5e shows the result of spectral deconvolution which is representative of the source spectrum of the 2013 Santa Cruz tsunami (painted area in Figure 5e). Based on Figure 5e, the
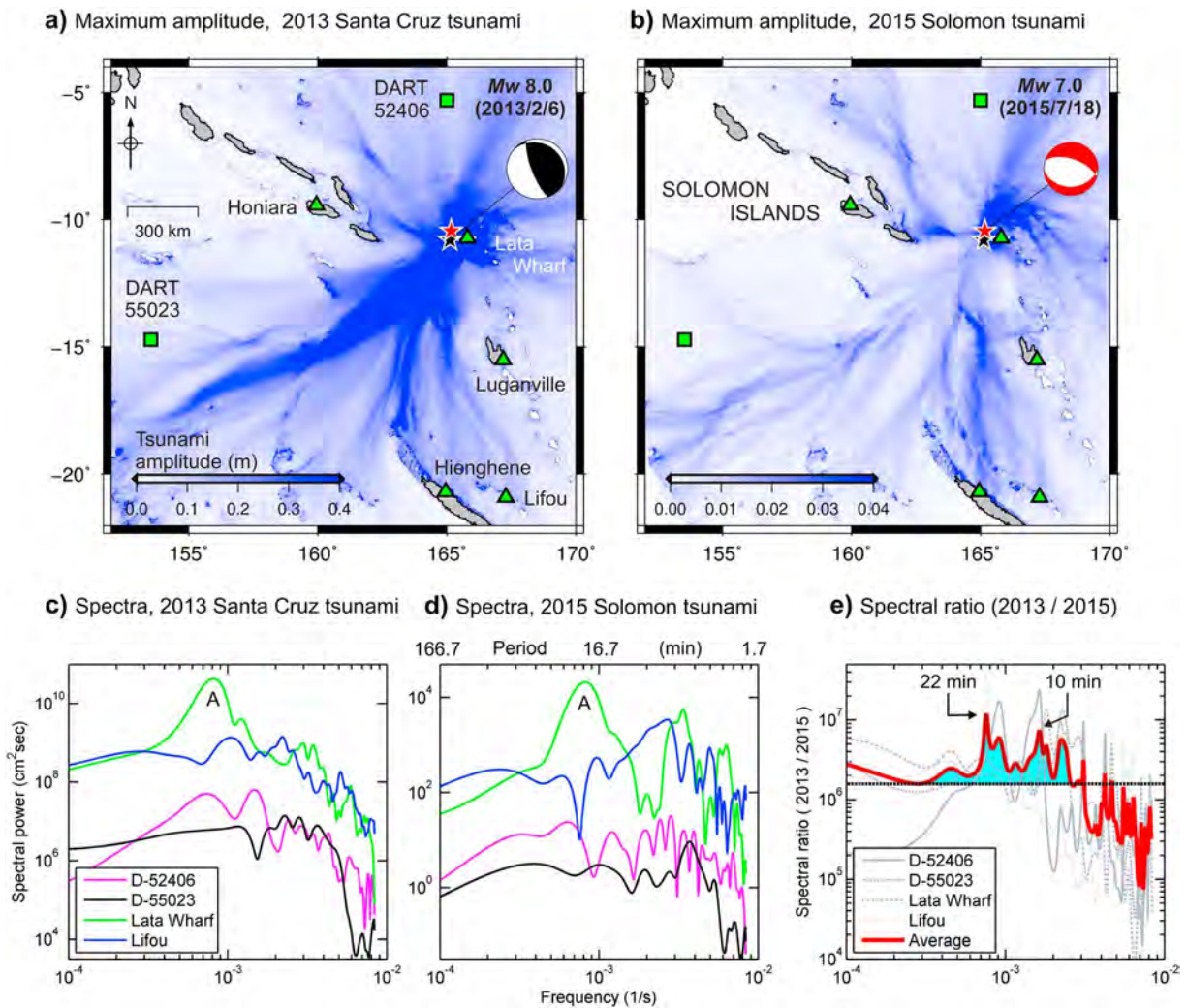
Figure 5. (a, b) Maximum simulated tsunami amplitudes for the 2013 and 2015 tsunamis. Source model used for the simulation of the 2013 tsunami is from *Lay et al.* [2013]. Note that color scale is different in these two panels. (c, d) Spectra for the tsunami waveforms of the 2013 Santa Cruz and 2015 Solomon Islands tsunamis. (e) Spectral ratio between the two tsunamis.

2013 Santa Cruz tsunami's energy is distributed in the period band of 7–50 min with two major peaks at 10 and 22 min. As the water depth around the source area is ~4500 m (Figure S9), these two peak periods imply source dimensions of ~60 km × ~140 km [using *Heidarzadeh and Satake* [2013], equation (3)] which is consistent with the source dimensions of ~65 km × ~135 km from teleseismic inversions of *Lay et al.* [2013] (Figure S9).

6. Comparison of Rupture Velocity Between Normal-Fault and Megathrust Earthquakes

Seismic wave analyses have shown that rupture velocities for shallow earthquakes are usually in the range of 1–4 km/s. For example, a V_r in the domain of 1.2–4.0 km/s was reported for the 11 March 2011 off-Tohoku earthquake using seismic data [e.g., *Simons et al.*, 2011; *Hayes*, 2011; *Yoshida et al.*, 2011]. The final model for the July 2015 normal-fault earthquake has a rupture velocity of 3.6 km/s which seems to be larger than that for megathrust earthquakes. Previous studies, applying joint tsunami and seismic data, revealed slower rupture velocities in the domain of 1.5–2.0 km/s for interplate megathrust earthquakes from various subduction zones [*Lay et al.*, 2009, 2013, 2014; *Gusman et al.*, 2015; *Heidarzadeh et al.*, 2015, 2016]. On the other hand, a relatively large rupture velocity of 3.5 km/s was reported for the January 2007 Kuril outer-rise normal-fault

earthquake [*Lay et al.*, 2009]. Although rupture velocity may vary depending on the earthquake depth and subduction zone, the data here may show that rupture velocity for normal-fault earthquakes ($V_r = 3.5$–3.6 km/s) tends to be larger than that for megathrust events ($V_r = 1.5$–2 km/s). This could be possibly explained by the rigidity at the earthquake source area: the more rigid the source area, the higher the rupture velocity [*Bilek and Lay*, 1999]. As normal-fault earthquakes occur within the plate, either in outer-rise region or on an overriding plate, where the rigidity of the crust is usually larger than that for plate interface; hence, the rupture velocity would be higher.

7. Conclusions

The 18 July 2015 M_w 7.0 Solomon Islands tsunamigenic normal-fault earthquake was investigated employing tsunami and teleseismic data analysis and was compared with the 6 February 2013 Santa Cruz M_w 8.0 earthquake and tsunami. Main results are the following:

1. A combined use of tsunami and teleseismic data led us to a model of the north dipping fault plane with rupture velocity of 3.6 km/s as the final model for the 2015 earthquake. The average slip was 0.6 m, and the large-slip area was 35 km (along strike) $\times$ 10 km (along dip). The seismic moment is 4.21×10^{19} Nm giving M_w 7.0.
2. Coulomb stress transfer and seismicity analyses indicate that the occurrence of the recent 2015 earthquake was possibly facilitated by the 2013 Santa Cruz earthquake.
3. The 2015 Solomon Islands tsunami serves as empirical Green's function for the 2013 Santa Cruz tsunami. Spectral deconvolution, assuming the 2015 tsunami as empirical Green's function, indicated the source periods of the 2013 tsunami as 10 and 22 min.
4. Results of this study combined with data from other subduction zones revealed that rupture velocity for intraplate normal-fault earthquakes ($V_r = 3.5$–3.6 km/s) tends to be larger than that for interplate megathrust earthquakes ($V_r = 1.5$–2 km/s).

References

Ammon, C. J., H. Kanamori, and T. Lay (2008), A great earthquake doublet and seismic stress transfer cycle in the central Kuril islands, *Nature*, *451*(7178), 561–565.

Bassin, C., G. Laske, and G. Masters (2000), The current limits of resolution for surface wave tomography in North America, *Eos Trans. AGU*, *81*, F897.

Beavan, J., X. Wang, C. Holden, K. Wilson, W. Power, G. Prasetya, M. Bevis, and R. Kautoke (2010), Near-simultaneous great earthquakes at Tongan megathrust and outer rise in September 2009, *Nature*, *466*(7309), 959–963.

Bilek, S. L., and T. Lay (1999), Rigidity variations with depth along interplate megathrust faults in subduction zones, *Nature*, *400*(6743), 443–446.

Chen, T., A. V. Newman, L. Feng, and H. M. Fritz (2009), Slip distribution from the 1 April 2007 Solomon Islands earthquake: A unique image of near-trench rupture, *Geophys. Res. Lett.*, *36*, L16307, doi:10.1029/2009GL039496.

Fritz, H. M., A. Papantoniou, L. Biukoto, A. Gilly, and Y. Wei (2014), The Solomon Islands tsunami of 6 February 2013 in the Santa Cruz Islands: Field survey and modeling, EGU General Assembly 2014, held 27 April–2 May, in Vienna, Austria.

Fritz, H. M., and N. Kalligeris (2008), Ancestral heritage saves tribes during 1 April 2007 Solomon Islands tsunami, *Geophys. Res. Lett. 35*, L01607, doi:10.1029/2007GL031654.

Fritz, H. M., et al. (2011), Insights on the 2009 South Pacific tsunami in Samoa and Tonga from field surveys and numerical simulations, *Earth Sci. Rev.*, *107*(1), 66–75.

Frohlich, C. (1992), Triangle diagrams: Ternary graphs to display similarity and diversity of earthquake focal mechanisms, *Phys. Earth Planet. Int.*, *75*(1), 193–198.

Fujii, Y., and K. Satake (2008), Tsunami sources of the November 2006 and January 2007 great Kuril earthquakes, *Bull. Seismol. Soc. Am.*, *98*(3), 1559–1571.

Geoware (2011), The tsunami travel times (TTT). [Available at http://www.geoware-online.com/tsunami.html.]

Gusman, A. R., Y. Tanioka, H. Matsumoto, and S. I. Iwasaki (2009), Analysis of the Tsunami generated by the great 1977 Sumba earthquake that occurred in Indonesia, *Bull. Seismol. Soc. Am.*, *99*(4), 2169–2179.

Gusman, A. R., S. Murotani, K. Satake, M. Heidarzadeh, E. Gunawan, S. Watada, and B. Schurr (2015), Fault slip distribution of the 2014 Iquique, Chile, earthquake estimated from ocean-wide tsunami waveforms and GPS data, *Geophys. Res. Lett.*, *42*, 1053–1060, doi:10.1002/2014GL062604.

Hartzell, S. H. (1978), Earthquake aftershocks as Green's functions, *Geophys. Res. Lett.*, *5*(1), 1–4, doi:10.1029/GL005i001p00001.

Hayes, G. P. (2011), Rapid source characterization of the 2011 M_w 9.0 off the Pacific coast of Tohoku earthquake, *Earth Planets Space*, *63*(7), 529–534.

Heidarzadeh, M., and K. Satake (2013), The 21 May 2003 tsunami in the Western Mediterranean Sea: Statistical and wavelet analyses, *Pure Appl. Geophys.*, *170*(9–10), 1449–1462.

Heidarzadeh, M., and K. Satake (2014), Excitation of basin-wide modes of the Pacific Ocean following the March 2011 Tohoku tsunami, *Pure Appl. Geophys.*, *171*(12), 3405–3419.

Heidarzadeh, M., A. R. Gusman, T. Harada, and K. Satake (2015), Tsunamis from the 29 March and 5 May 2015 Papua New Guinea earthquake doublet (M_w 7.5) and tsunamigenic potential of the New Britain trench, *Geophys. Res. Lett.*, *42*, 5958–5965, doi:10.1002/2015GL064770.

Heidarzadeh, M., S. Murotani, K. Satake, T. Ishibe, and A. R. Gusman (2016), Source model of the 16 September 2015 Illapel, Chile M_w 8.4 earthquake based on teleseismic and tsunami data, *Geophys. Res. Lett.*, *43*, 643–650, doi:10.1002/2015GL067297.

Intergovernmental Oceanographic Commission, IHO, and BODC (2003), Centenary edition of the GEBCO Digital Atlas, published on CD-ROM on behalf of the Intergovernmental Oceanographic Commission and the International Hydrographic Organization as part of the General Bathymetric Chart of the Oceans, British Oceanographic Data Centre, Liverpool, U. K.

Ishibe, T., K. Satake, S. Sakai, K. Shimazaki, H. Tsuruoka, Y. Yokota, S. Nakagawa, and N. Hirata (2015), Correlation between Coulomb stress imparted by the 2011 Tohoku-Oki earthquake and seismicity rate change in Kanto, Japan, *Geophys. J. Int.*, *201*(1), 112–134.

Ishibe, T., K. Shimazaki, K. Satake, and H. Tsuruoka (2011), Change in seismicity beneath the Tokyo metropolitan area due to the 2011 off the Pacific coast of Tohoku earthquake, *Earth Planets Space*, *63*(7), 731–735.

Kato, A., S. Sakai, and K. Obara (2011), A normal-faulting seismic sequence triggered by the 2011 off the Pacific coast of Tohoku earthquake: Wholesale stress regime changes in the upper plate, *Earth Planets Space*, *63*(7), 745–748.

Kennett, B. L. N., E. R. Engdahl, and R. Buland (1995), Constraints on seismic velocities in the Earth from travel times, *Geophys. J. Int.*, *122*, 108–124.

Kikuchi, M., and H. Kanamori (1991), Inversion of complex body waves—III, *Bull. Seismolo. Soc. Am.*, *81*(6), 2335–2350.

Koketsu, K., et al. (2011), A unified source model for the 2011 Tohoku earthquake, *Earth Planet. Sci. Lett.*, *310*(3), 480–487.

Lay, T., H. Kanamori, C. J. Ammon, A. R. Hutko, K. Furlong, and L. Rivera (2009), The 2006–2007 Kuril Islands great earthquake sequence, *J. Geophys. Res.*, *114*, B11308, doi:10.1029/2008JB006280.

Lay, T., L. Ye, H. Kanamori, Y. Yamazaki, K. F. Cheung, and C. J. Ammon (2013), The February 6, 2013 M_w 8.0 Santa Cruz Islands earthquake and tsunami, *Tectonophysics*, *608*, 1109–1121.

Lay, T., H. Yue, E. E. Brodsky, and C. An (2014), The 1 April 2014 Iquique, Chile, M_w 8.1 earthquake rupture sequence, *Geophys. Res. Lett.*, *41*, 3818–3825, doi:10.1002/2014GL060238.

Murotani, S., K. Satake, and Y. Fujii (2013), Scaling relations of seismic moment, rupture area, average slip, and asperity size for $M \sim 9$ subduction-zone earthquakes, *Geophys. Res. Lett.*, *40*, 5070–5074, doi:10.1002/grl.50976.

Nakanishi, I., and H. Kanamori (1984), Source mechanisms of twenty-six large, shallow earthquake (M_S 6.5) during 1980 from *P*-wave first motion and long-period Rayleigh wave data, *Bull. Seismolo. Soc. Am.*, *74*(3), 805–818.

Newman, A. V., L. Feng, H. M. Fritz, Z. M. Lifton, N. Kalligeris, and Y. Wei (2011), The energetic 2010 M_W 7.1 Solomon Islands tsunami earthquake, *Geophys. J. Int.*, *186*(2), 775–781.

Okada, Y. (1985), Surface deformation due to shear and tensile faults in a half-space, *Bull. Seismolo. Soc. Am.*, *75*, 1135–1154.

Okal, E. A., et al. (2010), Field survey of the Samoa tsunami of 29 September 2009, *Seismol. Res. Lett.*, *81*(4), 577–591.

Rabinovich, A. B. (1997), Spectral analysis of tsunami waves: Separation of source and topography effects, *J. Geophys. Res.*, *102*(C6), 12,663–12,676, doi:10.1029/97JC00479.

Rabinovich, A. B., R. N. Candella, and R. E. Thomson (2013), The open ocean energy decay of three recent trans-Pacific tsunamis, *Geophys. Res. Lett.*, *40*, 3157–3162, doi:10.1002/grl.50625.

Rabinovich, A. B., L. I. Lobkovsky, I. V. Fine, R. E. Thomson, T. N. Ivelskaya, and E. A. Kulikov (2008), Near-source observations and modeling of the Kuril Islands tsunamis of 15 November 2006 and 13 January 2007, *Adv. Geosci.*, *14*, 105–116.

Romano, F., I. Molinari, S. Lorito, and A. Piatanesi (2015), Source of the 6 February 2013 M w 8.0 Santa Cruz Islands Tsunami, *Nat. Hazards Earth Syst. Sci.*, *15*, 1371–1379.

Satake, K. (1987), Inversion of tsunami waveforms for the estimation of a fault heterogeneity: Method and numerical experiments, *J. Phys. Earth*, *35*(3), 241–254.

Satake, K. (1995), Linear and nonlinear computations of the 1992 Nicaragua earthquake tsunami, *Pure Appl. Geophys.*, *144*, 455–470.

Satake, K. (1988), Effects of bathymetry on tsunami propagation: Application of ray tracing to tsunamis, *Pure Appl. Geophys.*, *126*(1), 27–36.

Simons, M., et al. (2011), The 2011 magnitude 9.0 Tohoku-Oki earthquake: Mosaicking the megathrust from seconds to centuries, *Science*, *332*(6036), 1421–1425.

Stein, R. S. (1999), The role of stress transfer in earthquake occurrence, *Nature*, *402*(6762), 605–609.

Stein, R. S., G. C. P. King, and J. Lin (1992), Change in failure stress on the southern San Andreas fault system caused by the 1992 magnitude = 7.4 Landers earthquake, *Science*, *258*, 1328–1332.

Tanaka, M., K. Asano, T. Iwata, and H. Kubo (2014), Source rupture process of the 2011 Fukushima-ken Hamadori earthquake: How did the two subparallel faults rupture?, *Earth Planets Space*, *66*(1), 1–8.

Tanioka, Y., R. Larry, and K. Satake (1997), What controls the lateral variation of large earthquake occurrence along the Japan Trench?, *Island Arc*, *6*, 261–266.

Taylor, F. W., R. W. Briggs, C. Frohlich, A. Brown, M. Hornbach, A. K. Papabatu, A. J. Meltzner, and D. Billy (2008), Rupture across arc segment and plate boundaries in the 1 April 2007 Solomons earthquake, *Nat. Geosci.*, *1*(4), 253–257.

Taylor, M. A., G. Zheng, J. R. Rice, W. D. Stuart, and R. Dmowska (1996), Cyclic stressing and seismicity at strongly coupled subduction zones, *J. Geophys. Res.*, *101*(B4), 8363–8381, doi:10.1029/95JB03561.

Wei, Y., H. M. Fritz, V. V. Titov, B. Uslu, C. Chamberlin, and N. Kalligeris (2015), Source models and near-field impact of the 1 April 2007 Solomon Islands tsunami, *Pure Appl. Geophys.*, *172*(3–4), 657–682.

Welch, P. (1967), The use of fast Fourier transform for the estimation of power spectra: A method based on time averaging over short, modified periodograms, *IEEE Trans. Audio Electroacoust.*, *AE-15*, 70–73.

Wessel, P., and W. H. F. Smith (1998), New, improved version of Generic Mapping Tools released, *Eos Trans. AGU*, *79*(47), 579, doi:10.1029/98EO00426.

Ye, L., T. Lay, H. Kanamori, and K. D. Koper (2016), Rapidly estimated seismic source parameters for the 16 September 2015 Illapel, Chile M_w 8.3 earthquake, *Pure Appl. Geophys.*, doi:10.1007/s00024-015-1202-y.

Yoshida, K., K. Miyakoshi, and K. Irikura (2011), Source process of the 2011 off the Pacific coast of Tohoku earthquake inferred from waveform inversion with long-period strong-motion records, *Earth Planets Space*, *63*(7), 577–582.

Zheng, G., R. Dmowska, and J. R. Rice (1996), Modeling earthquake cycles in the Shumagin subduction segment, Alaska, with seismic and geodetic constraints, *J. Geophys. Res.*, *101*(B4), 8383–8392, doi:10.1029/95JB03461.